



# Observations of Rapidly Growing Whistler Waves in Front of Space Plasma Shock due to Resonance Interaction between Fluctuating Electron Velocity Distributions and Electromagnetic Fields

Jiansen He<sup>1</sup>, Xingyu Zhu<sup>1</sup>, Qiaowen Luo<sup>2</sup>, Chuanpeng Hou<sup>1</sup>, Daniel Verscharen<sup>3</sup>, Die Duan<sup>1</sup>, Wenya Li<sup>4</sup>, Jinsong Zhao<sup>5</sup>, Tiejian Wang<sup>6</sup>, Daniel B. Graham<sup>7</sup>, Qiugang Zong<sup>1</sup>, and Zhonghua Yao<sup>8</sup>

<sup>1</sup>School of Earth and Space Sciences, Peking University, Beijing 100871, People's Republic of China; [jshept@pku.edu.cn](mailto:jshept@pku.edu.cn)

<sup>2</sup>School of Atmospheric Sciences, Sun Yat-sen University, Zhuhai 519000, People's Republic of China

<sup>3</sup>Mullard Space Science Laboratory, University College London, Dorking RH5 6NT, UK

<sup>4</sup>State Key Laboratory of Space Weather, National Space Science Center, Chinese Academy of Sciences, Beijing 100190, People's Republic of China

<sup>5</sup>Purple Mountain Observatory, Chinese Academy of Sciences, Nanjing 210008, People's Republic of China

<sup>6</sup>School of Earth Science, Yunnan University, Kunming 650500, People's Republic of China

<sup>7</sup>Swedish Institute of Space Physics, Uppsala SE-75121, Sweden

<sup>8</sup>Key Laboratory of Earth and Planetary Physics, Institute of Geology and Geophysics, Chinese Academy of Sciences, Beijing 100029, People's Republic of China

Received 2021 November 22; revised 2022 October 3; accepted 2022 October 13; published 2022 December 19

## Abstract

The whistler-mode wave extending from the fast-magnetosonic wave branch is a fundamental perturbation of electromagnetic fields and plasmas in various environments including planetary space, laboratory, and astrophysics. The origin and evolution of the waves is a long-standing question due to the limited instrumental capability in resolving highly variable plasma and electromagnetic fields. Here, we analyze observational data with a high time resolution from the Magnetospheric Multiscale spacecraft in front of the terrestrial bow shock (e.g., foreshock). We develop a novel approach to extract the three-dimensional fluctuating electron velocity distributions ( $\delta f_e(\mathbf{V})$ ) from their background ( $f_{e0}(\mathbf{V})$ ), and have successfully captured the coherent resonance between fluctuating electrons ( $\delta f_e(\mathbf{V})$ ) and wavelike electromagnetic fields ( $\delta \mathbf{B}$ ,  $\delta \mathbf{E}$ ) at an unprecedentedly high frequency ( $>1$  Hz) for investigating wave–particle interactions. We provide that the unstable whistler wave grows rapidly over a timescale that is much shorter than the proton gyro-period. Regarding the energy origin for the waves, we find the ion distributions consisting of the solar wind ion flows and the ion beams reflected from the shock play crucial roles in providing the free energy and determining the eigenmode disturbances of fields and electrons. The quantification of wave growth rate and the characterization of wave–particle interactions for the instability driver can significantly advance the understandings of wave evolution and energy conversion between multisource multispecies particles and wave electromagnetic fields.

*Unified Astronomy Thesaurus concepts:* [Space plasmas \(1544\)](#); [Planetary bow shocks \(1246\)](#); [Solar wind \(1534\)](#)

*Supporting material:* animations

## 1. Introduction

The emission, propagation, and dissipation of plasma waves are fundamental processes in planetary space, interplanetary space, and beyond (Bruno & Carbone 2013; Le et al. 2013; Burch et al. 2016; Howes 2017; Narita 2018; Verscharen et al. 2019; Shan et al. 2020; Zong et al. 2020), and are ranked as one of the key objectives by various space exploration programs (Burch et al. 2016; Fox et al. 2016). The growth and dissipation of wavelike turbulence is a key consequence of energy conversion between fields and particles, which have been a research focus of the space physics community for decades (Gary 1993). The growth of waves could lead to the formation of shocklet or shock structures (Tsurutani et al. 1989). In previous literature, the instability for plasma waves is estimated by calculating the growth rate according to linear plasma theory with a predefined background plasma state and magnetic field as the observational input (Bale et al. 2009; Zhao et al. 2019). A direct examination of wave growth rate from spacecraft observations is crucial to validate the theoretical studies. The key barrier to obtain direct observational

evidence of wave growth is the limited resolving capability of space instruments, which have a breakthrough due to the successful launch of the Magnetospheric Multiscale (MMS) mission. MMS provides state-of-the-art high-quality measurements of electromagnetic fields and of the particle species by the FIELDS (Torbert et al. 2016) and Fast Plasma Investigation (Pollock et al. 2016) instruments, respectively.

The endeavors dedicated to diagnosing field–particle interactions have been recently arousing wide attention and significant concerns. Landau damping of kinetic Alfvén waves is highlighted by the observed correlation between the electron velocity distribution function and the parallel electric field (Gershman et al. 2017; Chen et al. 2019). Phase relations between wave fields and ion differential energy flux were observed, and the energy is suggested to transfer from ions to ion cyclotron waves (Kitamura et al. 2018). The spectra of the turbulence dissipation rate were provided for ion cyclotron waves and kinetic Alfvén waves in magnetosheath turbulence (He et al. 2020). However, these recent investigations are limited to low frequencies, and have never exceeded the ion gyro-frequency. The growth of whistler waves occurs at higher frequencies, which are ubiquitous and crucial for understanding high-frequency kinetic physics in multiple plasma environments (Wilson et al. 2013; Stansby et al. 2016). For whistler waves, the correlated change of the electron velocity

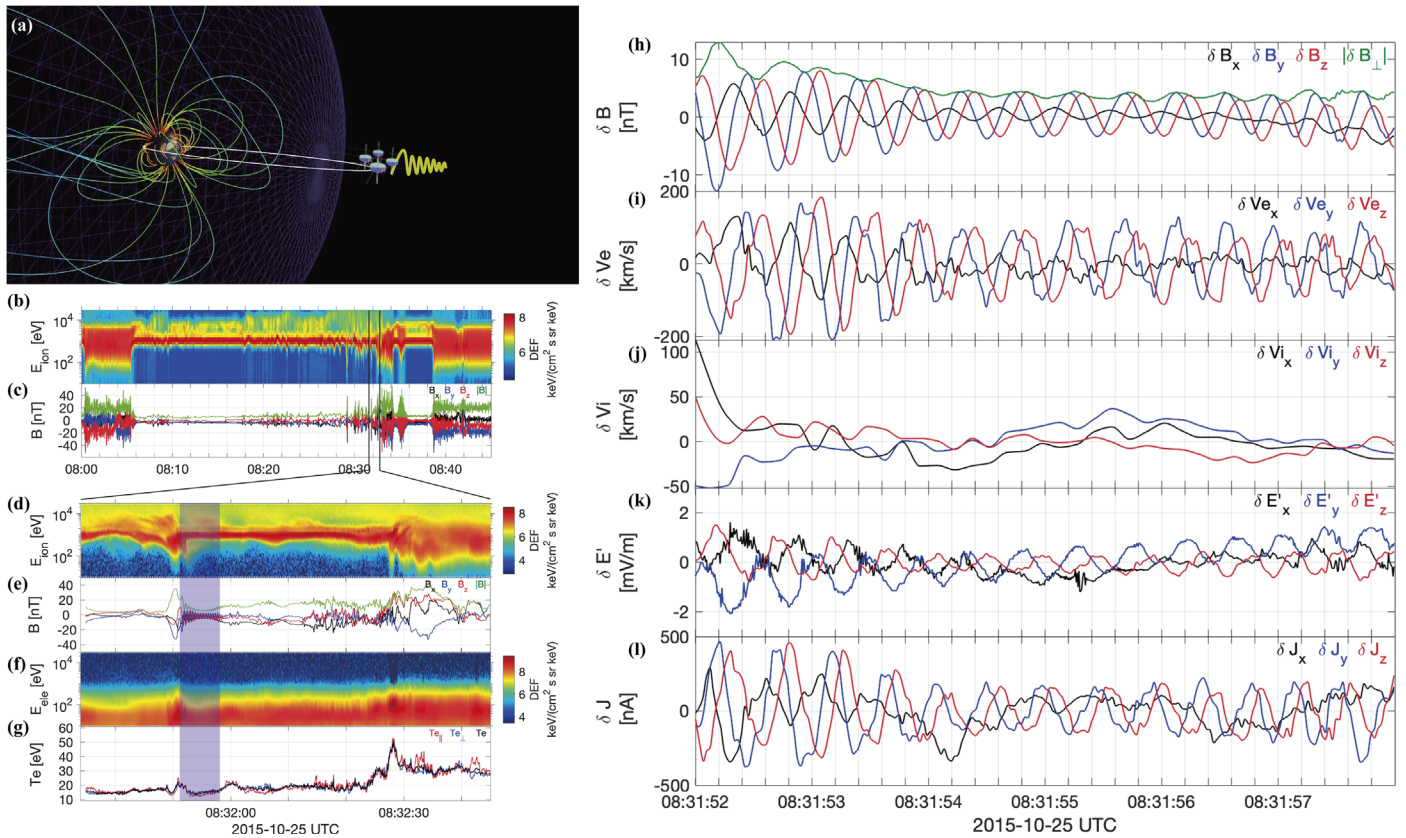


**Figure 1.** The MMS spacecraft outside Earth’s bow shock observe an event of large-amplitude whistler waves. (a) Sketch of particles and waves measured by MMS in front of the bow shock. The elements displayed in order outward from the Earth at the center are the magnetic lines of the geo-magnetosphere (color coded with magnetic field strength), the bow shock (semitransparent purple surface), the four MMS satellites, and whistler waves (yellow curves). (b) Ion energy spectrum in a prolonged interval involving the outbound and inbound bow shock crossings. (c) Magnetic field components in the same prolonged interval. (d) Ion energy spectrum in a shorter subinterval but still including the event marked by the shaded area. (e) Magnetic field components in the same subinterval. (f) Electron energy spectrum in the same subinterval. (g) Electron temperatures ( $T_{e,\parallel}$ ,  $T_{e,\perp}$ , and dimensional averaged  $T_e$ ) in the same subinterval. (h) Oscillations of the magnetic field ( $\delta B$ ) during the wave event. (i) Correlated oscillations of the electron fluid velocity ( $\delta V_e$ ) during the wave event. (j) Weak oscillations of the ion fluid velocity ( $\delta V_i$ ) during the wave event. (k) Oscillations of the electric field in the ion mean bulk flow frame ( $\delta E'$ ) during the wave event. (l) Oscillations of the current density ( $\delta J$ ) during the wave event.

distribution associated with the fluctuating wave electromagnetic fields has not been observed before, which is the primary goal of this work differing from previous studies. We target the foreshock region to investigate the growing process of whistler waves, since the plasma number density is sufficiently high for a detection at the timescale of electron gyro-motion and the magnetic field is weak enough for the gyro-motion to be captured by the detector recording. As a result, we reveal the comprehensive process of the field–particle interaction at a high measurement cadence, manifesting the ongoing rapid growth of whistler waves, which finally evolve to large amplitudes and contribute to shocklet formation. The field–particle coupling for whistler waves of this work is a crucial constituent of the collisionless shock physics, especially for the energy deposit and conversion of a supercritical shock.

## 2. Observational Analysis

### 2.1. Observation of Whistler Waves as Precursor Signal in Foreshock

MMS traveled in the upstream region of the terrestrial bow shock at 08:31 UT on 2015 October 25 (Figure 1(a)). Supercritical shocks like the Earth’s bow shock are typical in the heliosphere when the supersonic solar wind is hindered by a planetary magnetosphere, forming foreshocks in their upstream

regions (Eastwood et al. 2005; Turner et al. 2020). Burst-mode measurements of the fields and particles with high quality and high cadence provide an opportunity to reveal the process of field–particle interactions. In Figure 1, we show the wave signatures of different measurement variables. In Figures 1(b) and (c), we display, for a prolonged time interval, the ion energy spectrum and the magnetic field vectors. The interval is sufficiently long to involve both the outbound and inbound crossings of the bow shock. To see the details of the wave event under study, we illustrate a shortened time interval of the ion energy spectrum, magnetic field vectors, electron energy spectrum, and electron temperatures in Figures 1(d)–(g). We note that the wave activity is adjacent to a magnetic pulse structure likely to be a shocklet/short large-amplitude magnetic structure (SLAMS; see Figures 1(d) and (e)), which is a typical structure in the foreshock and believed to nonlinearly evolve from the foreshock ultra-low-frequency (ULF) waves (Hada et al. 1987; Tsubouchi & Lembege 2004). The nature of most ULF waves could be either Alfvénic for the nearly incompressible cases or associated with oblique magnetosonic-whistler waves for the magnetic compressible cases (Wilson 2016).

The magnetic field vectors oscillate in phase with the electron bulk velocities (Figures 1(h) and (i)), and both of them rotate quasi-circularly in the  $L$ – $M$  plane in LMN coordinates (Figure 2). The LMN coordinate system is obtained by

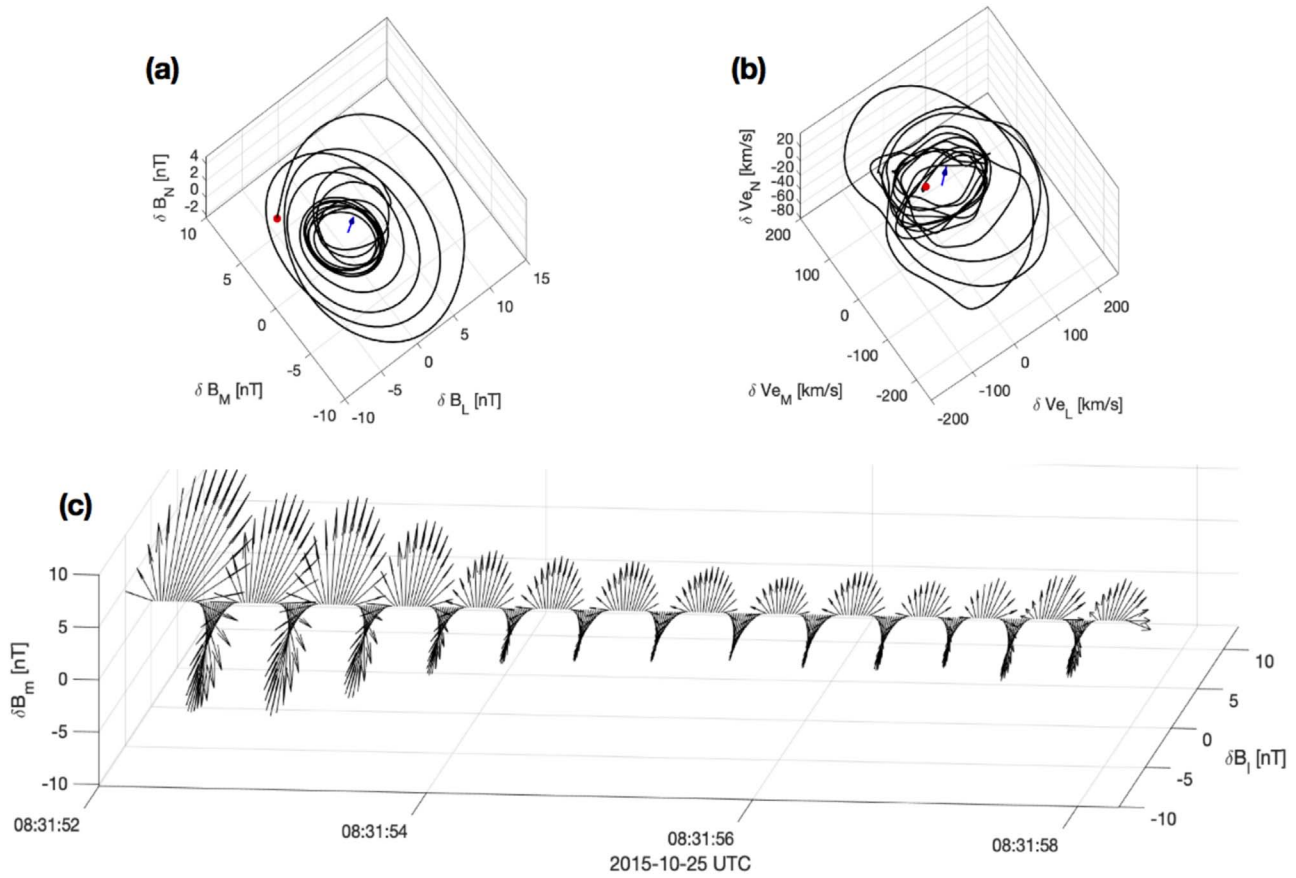


**Figure 2.** Magnetic field and electron fluid velocity disturbances show right-handed polarization, which is typical for whistler waves. (a)–(b) Hodograms of the fluctuating magnetic field vectors ( $\delta \mathbf{B}$ ) and the electron fluid velocity vectors ( $\delta \mathbf{V}_e$ ) in LMN coordinates as transformed from Geocentric Solar Ecliptic (GSE) coordinates through MVA. (c) Arrangement of fluctuating magnetic field vector ( $\delta \mathbf{B}$ ) in chronological order.

applying the minimum variance analysis (MVA) technique to the magnetic field vector sequences, and applied as a coordinate transformation to the electron bulk velocity vectors. On the contrary, the ions’ bulk velocity exhibits a much weaker oscillation leaving the current density oscillation mainly contributed by electrons’ bulk velocity (Figure 1(j)). The electric field vectors also experience quasiperiodic oscillations (Figure 1(k)). Note that, we use  $-\mathbf{V}_e \times \mathbf{B}$  to approximate the  $E_z$  component since the quality of  $E_z$  as measured by the axial double probe instrument is not as good as  $E_x$  and  $E_y$ , measured by the spin-plane double probe instrument. This approximation would somewhat underestimate the growth rate but does not affect the conclusion.

The fluctuating electric field is an indispensable building block in the resonance between waves and particles. The fluctuating electric field resonates with the disturbed electron phase space density so that the first-order moment integral of the electron phase space density and its corresponding current (Figure 1(l)) revolve around the background magnetic field. The spatial gradient of the associated wave current along the wavevector direction leads to the appearance and growth of the fluctuating magnetic field. The fluctuating magnetic field changes with time, and occurs self-consistently with the evolution of the fluctuating electric field through Faraday’s law.

We find the wave propagation in the solar-wind flow frame to be in the upwind/sunward direction, based on both the multispacecraft timing method (Paschmann & Daly 1998) and the singular-value decomposition (SVD) method

(Santolik et al. 2003). According to the analysis based on the electromagnetic SVD method (Santolik et al. 2003), the wave propagation angle is estimated to be about  $120^\circ$ , the frequency in the plasma reference frame is about 17 Hz, and the frequency in the spacecraft frame is about 2.5 Hz, which is lower due to the upstream propagation of waves against the flow. Therefore, we identify that the wave activity is associated with quasi-parallel right-hand polarized whistler waves, which changes to a left-hand polarization in the spacecraft frame due to the Doppler-shift effect. The waves’ relative amplitude is large ( $|\delta B|/B_0 > 1$ ), indicating a nonlinear state. Quasi-parallel propagating whistler waves with constant magnitudes of the transverse bulk velocity and magnetic field fluctuations are solutions of the full nonlinear multifluid equations for all wave amplitudes (Marsch & Verscharen 2011). Therefore, we can use the theoretical prediction from the linear plasma wave theory to investigate the essential physics behind our observations.

## 2.2. Observation of Field–Particle Correlation for the Whistler Waves

In the Earth-centered reference frame, the observed ion velocity distribution function ( $f_i$ ) consists of two distinct populations: an earthward core population of solar-wind ions and an anti-earthward beam population of ions reflected from the bow shock (Figures 3(a1) and (a2)). In this case, the core part of the reflected protons travels upstream in the spacecraft reference frame at a speed below the solar-wind speed. As a basic phenomenon, the relative drift speed between the

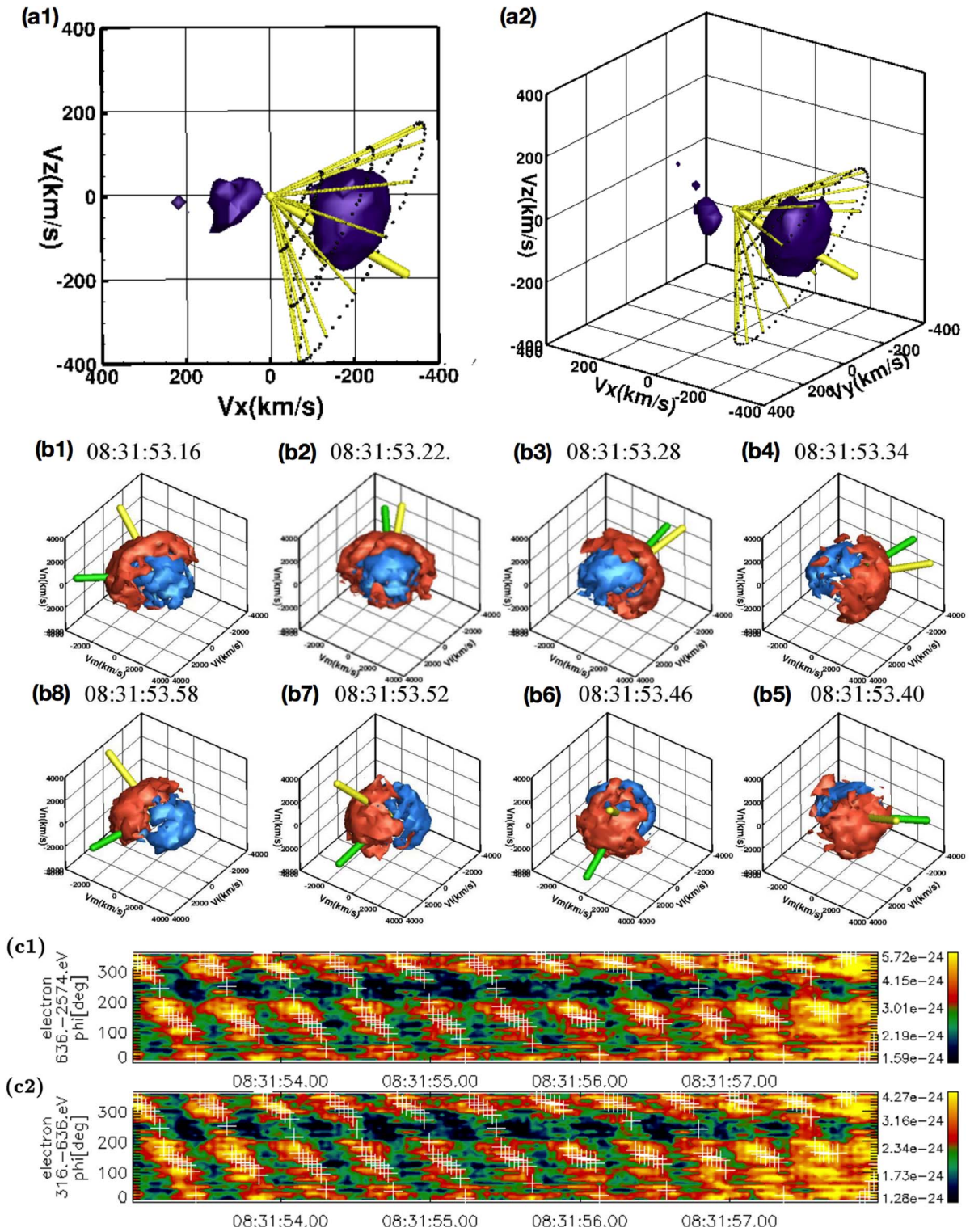


**Figure 3.** Ion-ion drift velocity distribution as the source of free energy to excite whistler waves. Clear correlations between the electromagnetic wave field and the electron velocity distributions show the field-particle interactions that drive the growth of whistler waves. (a1)–(a2) Ion velocity distribution in the GSE coordinates characterized by a pattern of “core-beam-drift”: the dark purple surfaces on the right and left sides of the origin show the solar-wind distribution as the core population and the shock-reflected ions as the beam population. The global mean magnetic field vector ( $\mathbf{B}_0$ ) and the local magnetic field vectors ( $\mathbf{B}_0 + \delta\mathbf{B}$ ) (disturbed by the wave fluctuations) are denoted by the thick and thin yellow sticks, respectively. (b1)–(b8) Disturbed electron velocity distributions in the LMN coordinates, with the red and blue isosurfaces representing the levels of positive and negative  $\delta f_e$  ( $\delta f_e = 10^{-25} \text{ cm}^{-6} \text{ s}^{-3}$ ), respectively. Rotate in phase with the wave electromagnetic field vectors ( $\delta\mathbf{B}$  by the yellow stick,  $\delta E'$  by the green stick) at subsecond periods. (c1)–(c2) We find a correlation between the azimuthal-angle distribution of electron phase space densities (colored background) and the azimuthal angles of the wave electric field vectors (white crosses). The animation proceeds through 10 rotations, corresponding to the time interval from 08:31:53.01 to 08:31:56.97.

(An animation of this figure is available.)

solar-wind protons and the reflected beam becomes smaller when the sampling location moves deeper into the foreshock region approaching the bow shock (e.g., von Althan et al. 2014). The whistler wave’s fluctuating magnetic field vectors are also illustrated in velocity space, gyrating like the ridges of an umbra around the ion core population. The non-Maxwellian ions are likely to drive plasma instabilities and excite waves. However, before this work, it still remains a long-lasting challenge to capture the growing process of wave activity since the essential field–particle interaction responsible for the energy transfer has yet to be revealed. What would happen to electrons for coupling under the condition of non-Maxwellian ions?

The oscillation of the disturbed electron velocity distribution function ( $\delta f_e$ ) as a perturbation related to the eigenmode reflects the key role of particles in the process of field–particle interactions. In line with the definition of the disturbed velocity distribution function adopted in linear Vlasov theory for plasma waves, we subtract the background velocity distribution function (VDF) as averaged over the wave period ( $f_{e,0}$ ) from the real-time measured VDF ( $f_e$ ) to get the disturbed VDF ( $\delta f_e = f_e - f_{e,0}$ ). We find that positive (red) and negative (blue)  $\delta f_e$  are located almost opposite to one another and gyrate in velocity space with the same period as that of the fluctuating electromagnetic fields ( $\delta E'$  (green),  $\delta B$  (yellow); Figures 3(b1)–(b8) and the associated online animation). Moreover, the electric field vector always points toward positive  $\delta f_e$  during the entire wave period, showing that the energy is transferred from the particles to the fields rather than the inverse. The good phase correlation between the  $\delta E'$ ’s azimuthal angle ( $\phi(\delta E')$ ) and the enhanced  $f_e$ ’s azimuthal angle ( $\phi(\text{enhanced} - f_e)$ ) is also illustrated in Figures 3(c1) and (c2).

### 3. Theoretical Interpretation

#### 3.1. From Field–Particle Correlation to Wave Growth

The Vlasov equation, which involves the background and disturbed velocity distributions as well as the disturbed electromagnetic fields, can be expressed as

$$\frac{\partial}{\partial t}(f_0 + \delta f) + \frac{q}{m}(\delta \mathbf{E} + \mathbf{V} \times \delta \mathbf{B}) \cdot \nabla_{\mathbf{V}}(f_0 + \delta f) + \mathbf{V} \cdot \nabla_{\mathbf{X}}(f_0 + \delta f) = 0, \quad (1)$$

where  $f_0$ ,  $\delta f$ ,  $\delta \mathbf{E}$ , and  $\delta \mathbf{B}$  are the background velocity distribution, the wave-disturbed velocity distribution, and the wave electric and magnetic fields, respectively. The electric field part in the Lorentz force is responsible for the energy transfer between fields and particles, while the magnetic field part contributes to the energy transfer of the particles themselves between the parallel and perpendicular directions. Therefore, the term  $\delta \mathbf{E} \cdot \nabla_{\mathbf{V}} \delta f$  is crucial for investigating the time-integrated effect of energy transfer between fields and particles. This term relates directly to the rate of change of the field energy and particles kinetic energy:

$$\begin{aligned} \frac{\partial}{\partial t} \left( \frac{\delta B^2}{2\mu_0} \right) &\sim - \int \frac{\partial}{\partial t} (f_0 + \delta f) V^2 d\mathbf{V} \\ &\sim -2 \frac{q}{|q|} \frac{|q|}{m} \int (\delta E_{\parallel} \delta f V_{\parallel} + \delta E_{\perp 1} \delta f V_{\perp 1} + \delta E_{\perp 2} \delta f V_{\perp 2}) d\mathbf{V}. \quad (2) \end{aligned}$$

Therefore, for  $\frac{q}{|q|} < 0$ , like in the case of electrons, if  $\langle (\delta \mathbf{E} \cdot \mathbf{V}) \delta f(\mathbf{V}) \rangle > 0$ , which means that the sense of correlation between  $\delta f$  and  $\delta \mathbf{E}$  is the same as the sense of correlation between  $\delta \mathbf{V}$  and  $\delta f$ , then magnetic field energy increases with time ( $\frac{\partial}{\partial t} \left( \left\langle \frac{\delta B^2}{2\mu_0} \right\rangle \right) > 0$ ).

#### 3.2. Formula to Measure Growth Rate Spectrum

Following the formula provided by He et al. (2019), the spectrum of energy conversion rate as a function of frequency reads as

$$\varepsilon_{\text{JE}} = \frac{1}{4} (\delta \tilde{\mathbf{J}} \cdot \delta \tilde{\mathbf{E}}^* + \delta \tilde{\mathbf{J}}^* \cdot \delta \tilde{\mathbf{E}}), \quad (3)$$

where  $\tilde{\mathbf{J}}$ ,  $\tilde{\mathbf{J}}^*$ ,  $\tilde{\mathbf{E}}$ , and  $\tilde{\mathbf{E}}^*$  represent the spectral coefficients and corresponding conjugate counterparts of  $\delta \mathbf{J}$  and  $\delta \mathbf{E}$ , respectively. Dividing  $\varepsilon_{\text{JE}}$  by the wave electromagnetic field energy density spectra, we obtain the following growth/damping rate spectrum,

$$\gamma = - \frac{1}{2} \frac{1}{4} \frac{(\delta \tilde{\mathbf{J}} \cdot \delta \tilde{\mathbf{E}}^* + \delta \tilde{\mathbf{J}}^* \cdot \delta \tilde{\mathbf{E}})}{|\delta \tilde{\mathbf{B}}|^2 / 2\mu_0 + \varepsilon_0 |\delta \tilde{\mathbf{E}}|^2 / 2}. \quad (4)$$

The time–frequency spectrum of field–particle energy transfer rate  $\varepsilon_{\text{JE}}(t, f)$  shows an evident strip near a frequency of 2 Hz (Figures 4(a) and (c)). According to the relation  $\varepsilon_{\text{JE}}(t, f) \sim \gamma \delta B^2$  (He et al. 2019), we obtain the time-averaged growth rate spectra ( $\gamma_{\parallel}(f)$ ,  $\gamma_{\perp}(f)$ , and  $\gamma_{\text{trace}}(f)$ ) as a function of frequency, manifesting that  $\gamma_{\perp}(f)$  and  $\gamma_{\text{trace}}(f)$  show a distinct bump standing out from the background of the zero growth rate spectrum (Figures 4(b) and (d)). Here,  $\gamma_{\text{trace}}(f)$  is the sum of  $\gamma_{\parallel}(f)$  and  $\gamma_{\perp}(f)$ , representing the total energy conversion rate in all three dimensions. We note that the first half of the time interval has a larger growth rate and a larger amplitude than the second half. Such a difference of wave activity between the first and second halves is owed to the difference in ion velocity distribution, which has a more pronounced ion–ion drift distribution in the first half.

#### 3.3. Full Set of Eigenmode Solutions Based on Plasma Wave Theory

We inherit from previous works and develop a new code package called ‘‘Plasma Kinetics Unified Eigenmode Solutions’’ (PKUES) to calculate the eigenmode fluctuations comprehensively under the observed plasma conditions. The set of parameters for the plasma conditions are listed as follows:  $\beta_{\parallel c} = 6.5$ ,  $T_{\perp c}/T_{\parallel c} = 10.2$ ,  $T_{\perp b}/T_{\parallel b} = 1.3$ ,  $n_b/n_c = 0.5$ ,  $T_{\parallel b}/T_{\parallel c} = 1.1$ ,  $v_d/c = -9.5 \times 10^{-4}$ ,  $w_{\parallel c}/c = 2.0 \times 10^{-4}$ ,  $T_{\parallel e}/T_{\parallel c} = 0.7$ ,  $T_{\perp e}/T_{\parallel e} = 1.1$ , where  $\beta_{\parallel c}$  is the proton core population’s parallel plasma beta value,  $T_{\perp c}/T_{\parallel c}$  is the proton core population’s thermal anisotropy,  $T_{\perp b}/T_{\parallel b}$  is the proton beam population’s thermal anisotropy,  $n_b/n_c$  is the density ratio of proton beam population to proton core population,  $T_{\parallel b}/T_{\parallel c}$  is the parallel temperature ratio between proton beam population and proton core population,  $v_d/c$  is the core–beam drift speed normalized to the light speed,  $w_{\parallel c}/c$  is the proton core population’s parallel thermal speed as normalized to the light speed,  $T_{\parallel e}/T_{\parallel c}$  is the parallel temperature ratio between the electron and proton core population, and  $T_{\perp e}/T_{\parallel e}$  is the electrons’ thermal anisotropy. We set the drift velocity ( $v_d$ ) to

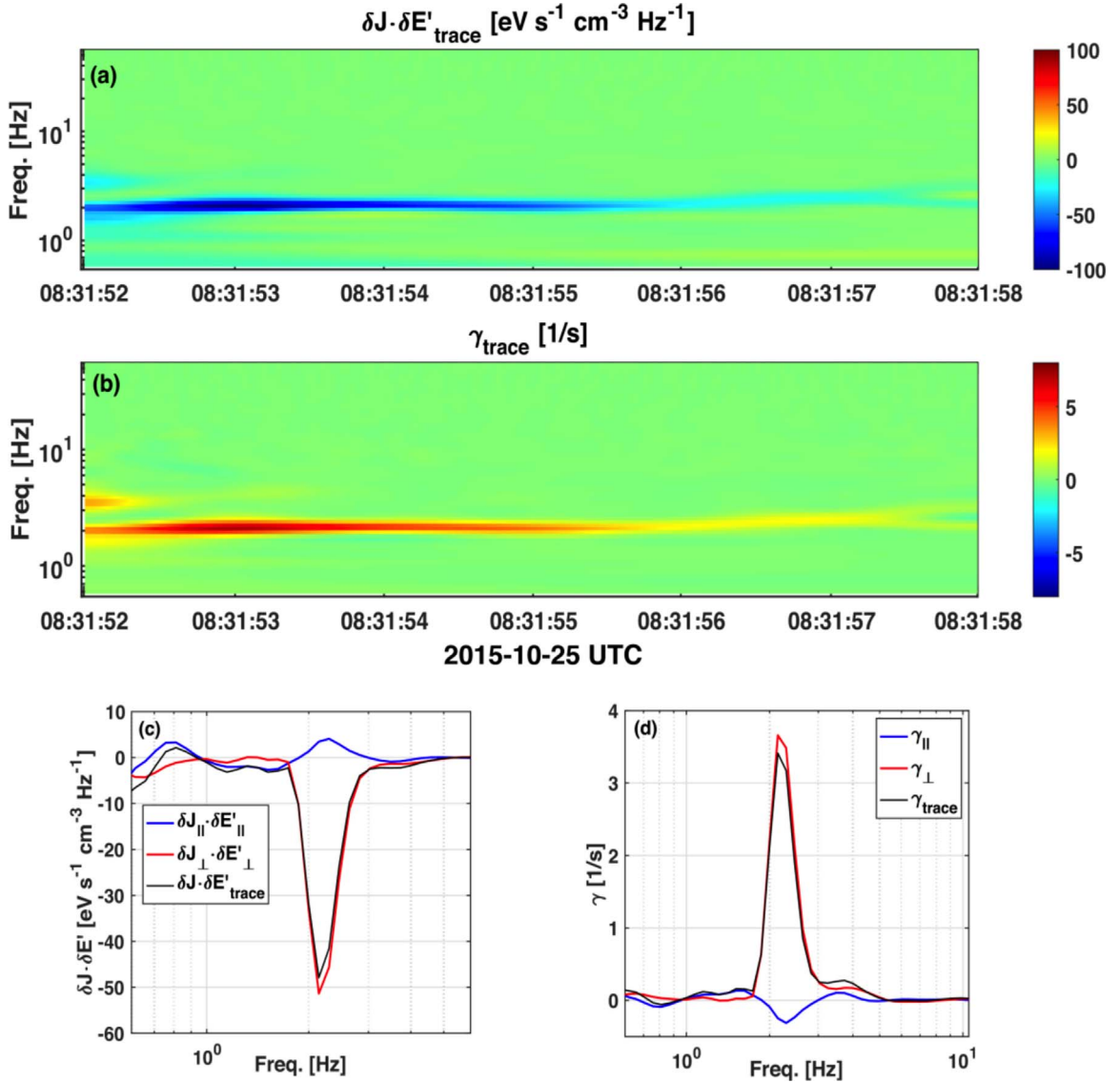


**Figure 4.** Evidence for ongoing enhancements of wave activity encountered by MMS. (a) Spectrum of  $\delta J \cdot \delta E'$  in a time–period diagram. (b) Spectrum of gamma, normalized growth rate, in the time–period diagram. (c) Frequency profiles of  $\delta J \cdot \delta E'$  including the trace and the components in the parallel and perpendicular directions. (d) Frequency profiles of gamma (normalized energy conversion rate).

be negative in the field-aligned coordinates because the observed drift velocity of reflected protons is antiparallel to the background magnetic field direction. Specifically, the  $x$  component of the background magnetic field and the drift velocity are negative and positive, respectively.

First, we use and modify the dispersion relation solver tool “Plasma Dispersion Relation Kinetics” (PDRK; Xie & Xiao 2016), which transforms the dispersion relation to a standard matrix eigenvalue problem of an equivalent linear system, to calculate all the possible solutions of eigenmodes at one time. Our modifications/improvements of PDRK consist of the following three steps: (1) We add the calculation of magnetic helicity and magnetic compressibility to help with the wave mode selection. (2) We distinguish different branches with different colors when displaying the dispersion relations of all wave modes. (3) We realize the function of interactive operation in the part of wave mode selection to select the solutions along the dispersion relation, avoiding manual input of the wave model solution.

We then manually choose the most plausible wave mode out of all eigenmode solutions according to the requirement that a selection of critical criteria agree with the observations: type of polarization (e.g., right-hand circular polarization), Doppler-shifted wave frequency (i.e., wave frequency in the spacecraft reference frame), transport ratio of fluctuation variables (e.g., large ratio of  $|\delta E|/|V_A \delta B|$ ), and sign of the growth rate (e.g., positive  $\gamma$  for the growth process). After determining the most consistent eigenmode with our observations, we then calculate the other fluctuation quantities, e.g., ion and electron fluctuating number densities and bulk velocity vectors, which are not addressed in the PDRK package. Similar to the “New Hampshire Dispersion Solver” (NHDS; Verscharen & Chandran 2018), we also calculate the disturbed ion and electron velocity distributions according to Chapter 10 in the book by Stix (1992). We incorporate the functions of both codes, PDRK and NHDS, and develop a new code package called “Plasma Kinetics Unified Eigenmode Solutions” (PKUES).

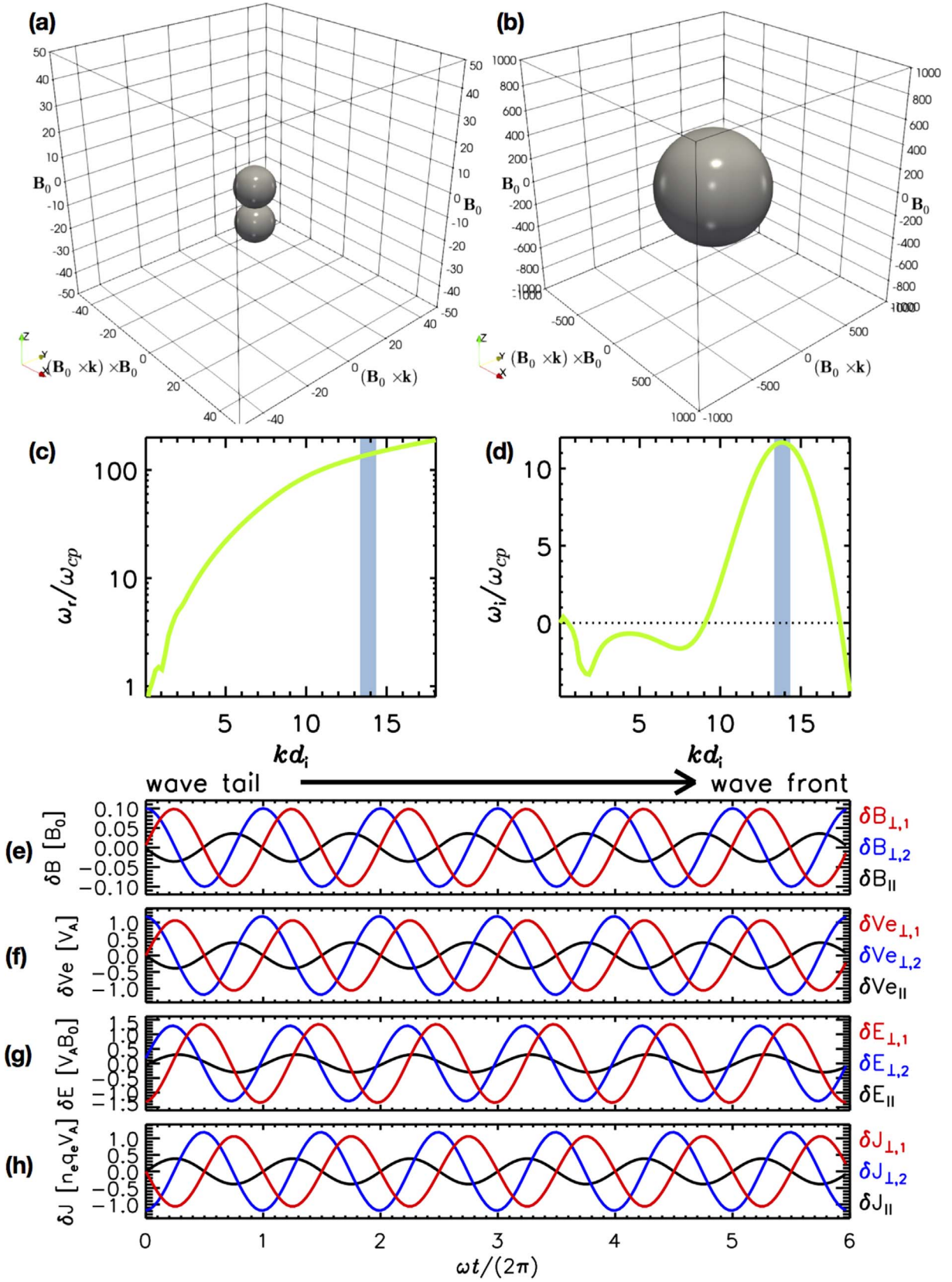


**Figure 5.** Eigenmode instability driven by non-Maxwellian ion phase space density as predicted from linear theory of plasma kinetics. (a) Ion phase space density with the integrated multiorder moments of the two populations. This theoretical result is similar to the results of our ion observations. (b) Electron phase space density. The integrated multiorder moments are also similar to those of our observations. (c) Dispersion relation and (d) growth rate profile of right-hand polarized whistler waves based on the given ion and electron background velocity distributions. (e)–(h) Time sequences of the disturbed magnetic field vectors, electron bulk velocity vectors, electric field vectors, and current density vectors.

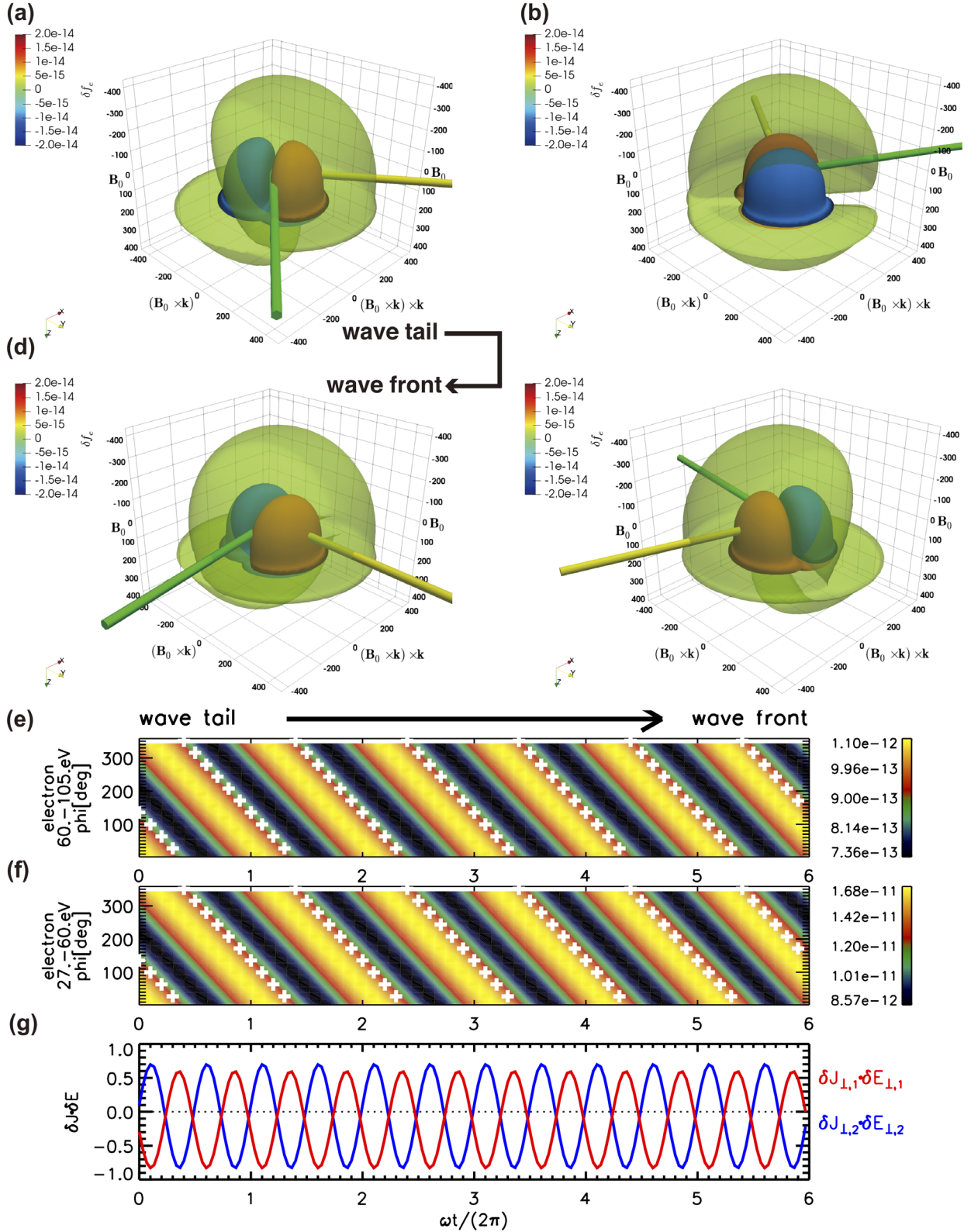


**Figure 6.** Analysis of field–particle correlations, which are the key underlying concept of secular wave–particle interactions and responsible for the growth of wave activity. (a)–(d) Correlations between perturbation of the electron phase space density ( $\delta f_e$ : red isosurface for  $\delta f_e > 0$ , blue isosurface for  $\delta f_e < 0$ , green isosurface for  $f_{e0} + \delta f_e$ ) and the electromagnetic field vectors (green stick for  $\delta E$ , yellow stick for  $\delta B$ ). (e)–(f) Correlation between the azimuthal angle of the fluctuating electron velocity distribution  $\phi_{\delta v_e}(t)$ . The angle of a temporally local maximum  $\delta f_e(t, \phi)$ , and the azimuth angle of the fluctuating electric field  $\phi_{\delta E}(t)$  serve as proxies. (g) Time sequences of the energy conversion rate from particles to electromagnetic fields (red for  $\delta J_{e,1,1} \cdot \delta E_{1,1}$ , blue for  $\delta J_{e,1,2} \cdot \delta E_{1,2}$ ). An animation of the rotating correlations between perturbation of the electron phase space density is available in the online journal. The animation proceeds through one complete rotation, corresponding to the time interval from  $\omega t = 0$  to  $\omega t = 2\pi$ .

(An animation of this figure is available.)

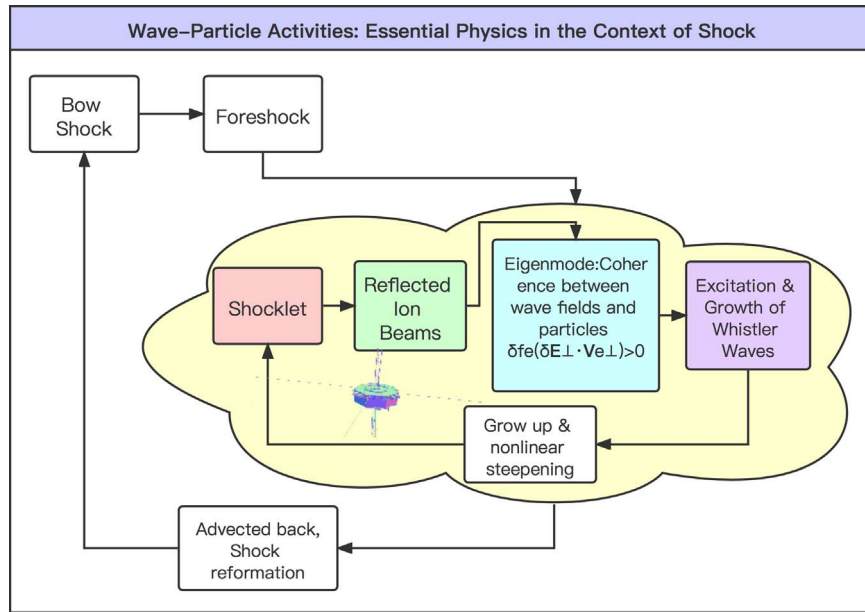


**Figure 7.** Fundamental physics of field–particle interactions taking place in the foreshock region of planetary bow shock. The drift between solar-wind ions and shock-reflected ions in velocity space is intrinsically unstable and determines the dominant eigenmode together that transfers the free energy between fields and particles. Perturbations of the electromagnetic fields and the electron velocity distribution associated with this dominant eigenmode couple to drive the whistler waves, which then evolve into nonlinear large amplitude and may contribute to the reformation of shocklet and shock.

### 3.4. Similar Field–Particle Correlation Reproduced in a Theoretical Model

The ion–ion drift instability and the associated excited whistler waves as witnessed by MMS are confirmed with the prediction from plasma wave theory (Gary 1991). Using background plasma parameters consistent with the observations, the ion VDF with an ion–ion core–beam drift and the electron VDF lead to whistler waves in linear theory with the properties as those observed in MMS (Figures 5(a) and (b)). Plasma wave theory predicts that the whistler wave is the unstable eigenmode in this case (see Figures 5(c) and (d) for its dispersion and growth rate relations). The wave fluctuations of the magnetic field, electric field, electron bulk velocity, and current density are sampled from the wave tail to the wave head (Figure 5(e)–(h)) for comparison with the observations in the spacecraft reference frame, where the whistler waves propagate upstream but are convected back by the solar-wind flow.

The theoretically predicted phase coherence between the gyrated disturbed electron velocity distribution ( $\delta f_e$ ) and the gyrated wave electromagnetic field vectors ( $\delta E'$  and  $\delta B$ ) is of great importance for understanding the relevant field–particle interactions (Figures 6(a)–(d) and the associated online animation). Again both the electric and magnetic field vectors ( $\delta E'$  and  $\delta B$ ) point toward positive  $\delta f_e$ , where the angle between  $\delta E'$  and  $\delta B$  is smaller than  $90^\circ$ , clearly suggesting the ongoing process of energy transfer from particles to fields and the enhancement of wave electromagnetic field energy. This particle-to-field energy transfer is also confirmed by the azimuthal-angle correlation between the enhanced  $f_e$  and the wave electric field  $\delta E'$  (Figures 6(e) and (f)), and the time sequence of  $\delta J \cdot \delta E'$ , which shows a negative level on average (Figure 6(g)).

## 4. Summary and Discussion

We take full advantages of the MMS satellite in measuring fields and particles with state-of-the-art high quality. We witness the growth of whistler waves at a high measurement cadence in

space plasmas. As the characteristic perturbations in the unstable whistler waves, we reveal the disturbed electron velocity distribution ( $\delta f_e$ ) and find it to be gyrating in phase with the disturbed electromagnetic field vectors, where the field vectors ( $\delta E'$  and  $\delta B$ ) point toward positive  $\delta f_e$ . We conclude that such phase correlations between  $\delta f_e$  and  $\delta E'$  are directly evidence of the energy transfer from particles to fields ( $\delta J \cdot \delta E' < 0$ ) that leads to the growth and emission of whistler waves. The wave frequency is estimated to be  $\omega_{SC} \sim 2.5$  Hz in the spacecraft reference frame, and  $\omega_{PL} \sim 16$  Hz in the plasma reference frame. The normalized growth rate is comparable in order of magnitude between the direct observation ( $\gamma_{obs} \sim 3$  Hz) and the theoretical prediction ( $\gamma_{theory} \sim 1$  Hz). We also obtain the spectrum of growth rate as a function of frequency directly from the in situ measurements. We identify and attribute the free-energy source for the whistler wave’s unstable growth to the proton’s “core–beam-drift” velocity distribution.

The scenario of whistler waves growth revealed in this work (Figure 7) helps us to understand the mystery of the origin of whistler waves, which are ubiquitous in various plasma environments. Our observational and theoretical studies are important to define a paradigm on how to explore field–particle couplings and how to quantify the coupling efficiency in collisionless plasmas. In principle, both ions and electrons are linked with and coupled through the electromagnetic fields. However, their dynamic evolution along with the wave fields is distinct from one another in this instability. As the source of free energy, the drifting ion beam population is scattered and decelerated by the Lorentz force as the second-order cross product of the disturbed ion beam fluid velocity with the disturbed magnetic field. The scattered and decelerated ion beam would modify the eigenmode’s polarizations, changing the phase relation between  $\delta f_e$  and  $\delta E'$ , hence saturating the growth of whistler waves. However, the ion beam’s disturbed velocity at the wave frequency cannot be well observed by the MMS plasma instrument, the angular resolution of which makes it difficult to achieve this goal. More-advanced space

missions dedicated to measuring the solar-wind plasma turbulence in the vast heliosphere with an ultrahigh angular resolution are required to accomplish the objective of revealing the mysteries of turbulence dissipation and cyclotron wave's prevalence.

We are grateful to the MMS team for their efforts in operating the measurements, calibrating the raw data, and making the calibrated data available to the public. We also thank the team of 3DView, which is maintained mainly by IRAP/CNES. Authors from China are supported by the National Key R&D Program of China (2021YFA0718600), by NSFC (42174194, 41874200, 42150105, 41974170, 42104157, and 41774186), by CNSA (D020301 and D050106), and by the Key Research Program of the Institute of Geology & Geophysics, CAS, Grant IGGCAS 201904. D.V. from UCL is supported by the STFC consolidated grants ST/S000240/1 and ST/W001004/1. About data availability: The MMS data set analyzed in this work is publicly available at <https://lasp.colorado.edu/mms/sdc/public/>. About code availability: The code for the tool package of "Plasma Kinetics Unified Eigenmode Solutions" (PKUES) is available at <https://github.com/PKU-Heliosphere/PKUES>.

#### ORCID iDs

Jiansen He  <https://orcid.org/0000-0001-8179-417X>  
 Xingyu Zhu  <https://orcid.org/0000-0002-1541-6397>  
 Qiaowen Luo  <https://orcid.org/0000-0001-7697-1186>  
 Chuanpeng Hou  <https://orcid.org/0000-0001-7205-2449>  
 Daniel Verscharen  <https://orcid.org/0000-0002-0497-1096>  
 Die Duan  <https://orcid.org/0000-0002-6300-6800>  
 Wenya Li  <https://orcid.org/0000-0003-1920-2406>  
 Jinsong Zhao  <https://orcid.org/0000-0002-3859-6394>  
 Tieyan Wang  <https://orcid.org/0000-0003-3072-6139>  
 Daniel B. Graham  <https://orcid.org/0000-0002-1046-746X>  
 Qiugang Zong  <https://orcid.org/0000-0002-6414-3794>  
 Zhonghua Yao  <https://orcid.org/0000-0001-6826-2486>

#### References

- Bale, S. D., Kasper, J. C., Howes, G. G., et al. 2009, *PhRvL*, **103**, 211101  
 Bruno, R., & Carbone, V. 2013, *LRSv*, **10**, 2  
 Burch, J. L., Moore, T. E., Torbert, R. B., & Giles, B. L. 2016, *SSRv*, **199**, 5  
 Chen, C. H. K., Klein, K. G., & Howes, G. G. 2019, *NatCo*, **10**, 740  
 Eastwood, J. P., Lucek, E. A., Mazelle, C., et al. 2005, *SSRv*, **118**, 41  
 Fox, N. J., Velli, M. C., Bale, S. D., et al. 2016, *SSRv*, **204**, 7  
 Gary, S. P. 1991, *SSRv*, **56**, 373  
 Gary, S. P. 1993, *Theory of Space Plasma Microinstabilities* (Cambridge: Cambridge Univ. Press)  
 Gershman, D. J., F-Vinas, A., Dorelli, J. C., et al. 2017, *NatCo*, **8**, 14719  
 Hada, T., Kennel, C. F., & Terasawa, T. 1987, *JGR*, **92**, 4423  
 He, J., Duan, D., Wang, T., et al. 2019, *ApJ*, **880**, 121  
 He, J., Zhu, X., Verscharen, D., et al. 2020, *ApJ*, **898**, 43  
 Howes, G. G. 2017, *PhPl*, **24**, 055907  
 Kitamura, N., Kitahara, M., Shoji, M., et al. 2018, *Sci*, **361**, 1000  
 Le, G., Chi, P. J., Blanco-Cano, X., et al. 2013, *JGRA*, **118**, 2809  
 Marsch, E., & Verscharen, D. 2011, *JPIPh*, **77**, 385  
 Narita, Y. 2018, *LRSv*, **15**, 2  
 Paschmann, G., & Daly, P. W. 1998, *ISSIR*, **1**  
 Pollock, C., Moore, T., Jacques, A., et al. 2016, *SSRv*, **199**, 331  
 Santolik, O., Parrot, M., & Lefeuvre, F. 2003, *RaSc*, **38**, 1010  
 Shan, L., Du, A., Tsurutani, B. T., et al. 2020, *ApJL*, **888**, L17  
 Stansby, D., Horbury, T. S., Chen, C. H. K., & Matteini, L. 2016, *ApJL*, **829**, L16  
 Stix, T. H. 1992, *Waves in Plasmas* (New York: Springer Science & Business Media)  
 Torbert, R. B., Russell, C. T., Magnes, W., et al. 2016, *SSRv*, **199**, 105  
 Tsubouchi, K., & Lembege, B. 2004, *JGRA*, **109**, A02114  
 Tsurutani, B. T., Smith, E. J., Brinca, A. L., Thorne, R. M., & Matsumoto, H. 1989, *P&SS*, **37**, 167  
 Turner, D. L., Liu, T. Z., Wilson, L. B., et al. 2020, *JGRA*, **125**, e27707  
 Verscharen, D., & Chandran, B. D. G. 2018, *RNAAS*, **2**, 13  
 Verscharen, D., Klein, K. G., & Maruca, B. A. 2019, *SoPh*, **16**, 5  
 von Alfthan, S., Pokhotelov, D., Kempf, Y., et al. 2014, *JASTP*, **120**, 24  
 Wilson, L. B. 2016, in *Low-Frequency Waves in Space Plasmas*, ed. A. Keiling et al. (Washington, DC: American Geophysical Union), 269  
 Wilson, L. B., Koval, A., Szabo, A., et al. 2013, *JGRA*, **118**, 5  
 Xie, H., & Xiao, Y. 2016, *PIST*, **18**, 97  
 Zhao, J., Wang, T., Shi, C., et al. 2019, *ApJ*, **883**, 185  
 Zong, Q., Escoubet, P., Sibeck, D., Le, G., & Zhang, H. 2020, *Dayside Magnetosphere Interactions* (Hoboken, NJ: Wiley)